

WORK FUNCTION MEASUREMENTS BY THE FIELD

EMISSION RETARDING POTENTIAL METHOD

Final Report  
NGR 38-010-001

**CASE FILE  
COPY**

submitted to  
The National Aeronautics and Space Administration  
Washington, D. C.

submitted by

L. W. Swanson

R. W. Swanson

W. A. Mackie

Linfield Research Institute  
Linfield College  
McMinnville, Oregon

December 1971

WORK FUNCTION MEASUREMENTS BY THE FIELD  
EMISSION RETARDING POTENTIAL METHOD

Final Report  
NGR 38-010-001

submitted to  
The National Aeronautics and Space Administration  
Washington, D.C.

submitted by  
L. W. Swanson  
R. W. Strayer  
W. A. Mackie

Linfield Research Institute  
Linfield College  
McMinnville, Oregon

December 1971

## ABSTRACT

Using the field emission retarding potential method true work functions have been measured for the following monocrystalline substrates: W(110), W(111), W(100), Nb(100), Ni(100), Cu(100), Ir(110) and Ir(111). The electron elastic and inelastic reflection coefficients from several of these surfaces have also been examined near zero primary beam energy.

# I.

## Work Function Measurements by the Field Emission Retarding Potential Method\*

by

R. W. Strayer<sup>†</sup>, W. Mackie, and L. W. Swanson

Linfield Research Institute, McMinnville, Oregon 97128

### INTRODUCTION

Of fundamental importance to the experimental and theoretical understanding of surfaces is the reliable measurement of its work function. Motivated by the advancing technology of electron emitting devices and, more recently, by progress in experimental and theoretical understanding of surfaces, an increasing number of measurements of clean, mono-crystal face work function have been reported. Primarily due to the perennial problem of surface purity and partly due to inadequacies in the theoretical description of the various modes of electron emission one finds an inordinate degree of disagreement in the literature values of work function. However, the rapid advance in the methodology of fabricating ultra pure metals along with the increasing number of ways of cleaning and sensitively detecting minute concentrations of surface impurities is gradually eliminating surface contamination as a major factor in arriving at a consensus as to the appropriate clean mono-crystal face work function values. A further problem of lesser importance

---

\*This work was supported by a grant from the National Aeronautics and Space Administration, Lewis Research Center, Cleveland, Ohio.

<sup>†</sup>In partial fulfillment of Ph.D. requirement at Oregon State University.

is that of maintaining a desired crystallographic orientation at the surface during the cleaning procedure; this problem can be detected by LEED and Laue x-ray analysis and occurs for relatively few materials.

It is in regards to the problem of the inadequacies of the existing models for various types of electron emission (e.g., thermionic, photo or field emission) to provide unambiguous values of mono-crystal face work function that has prompted this work. Here we are concerned not with contact potential difference measurement but rather with absolute (or true) work function.

The primary electron emission processes whereby work function values of the emitter can be theoretically obtained are thermionic, photo electric and field emission. The assumptions, limitations and applicability of each of these methods for obtaining work function values have been adequately described in the literature. Suffice it to say that the Sommerfeld free electron model, which is the basic model utilized by the experimentalist for most electron emission processes, is severely strained in its application to a wide variety of non-free electron refractory metal emitters. This limitation is succinctly described for thermionic, field and photo electric emission by Itskovich.<sup>1</sup> Recent field emission energy distribution measurements have given dramatic experimental evidence as to the inability of the Sommerfeld based Fowler-Nordheim theory to explain the results from all crystallographic directions of tungsten, molybdenum and copper emitters.<sup>2,3,4</sup> Besides the fundamental problem of model applicability, a host of minor complex effects

such as the temperature dependence of the work function, variable reflection coefficients and the Schottky effect must be carefully incorporated into the theoretical framework of the emission process.

A method of measuring the true work function of an electron collector surface which circumvents most, if not all, of the above mentioned difficulties is the field electron retarding potential (FERP) method. The FERP approach to work function studies, introduced many years ago by Henderson<sup>5</sup>, has been largely neglected with the exception of recent studies of polycrystal surfaces by Holscher<sup>6</sup> and Kleint.<sup>7</sup> Yet this method and an experimentally complex adaptation of the Shelton method<sup>8</sup> are the only ways by which non-relative work functions of an electron collector surface can be measured. As will be shown in the following section, the success of the FERP method rests on the theoretical and experimentally verifiable fact that the voltage threshold for collection of field emitted electrons occurs at the Fermi level  $E_f$  at  $0^\circ\text{K}$  or can be described by a Boltzman tail, i. e.,  $\exp(E_f - E)/kT$ , at temperature  $T$ . The several experimental studies of the total energy distribution (TED) now in the literature<sup>2, 9, 10</sup>, provide a firm basis for the validity of the preceding fact; also if the appropriate crystallographic direction of a refractory metal emitter is employed, the free electron based Fowler-Nordheim model of field emission is adequate for this application.

In the following sections we shall describe the theoretical basis of the FERP method, its experimental application to the measurement

of mono-crystal face work functions, and the results obtained from several substrates. An interesting and useful fallout from the experimental approach described here is the ability to accurately measure the elastic and inelastic reflection coefficient for impinging electrons to near zero volts energy.

### THEORETICAL CONSIDERATIONS

The expression for the differential field emitted current  $dI_c$  between energy  $\epsilon$  and  $\epsilon + d\epsilon$  (where  $\epsilon = E - E_f$ ) in the case of a free electron model is given as follows:

$$dI_c/d\epsilon = I_o e^{\epsilon/d} / [(1 + e^{\epsilon/pd})d] \quad (1)$$

where  $p = kT/d$  is a dimensionless parameter. The value  $d$  is given by

$$d = \hbar e F / 2(2m\phi_e)^{1/2} t(y) = 0.976 F / \phi_e^{1/2} t(y) \text{ (eV)} \quad (2)$$

where the electric field  $F$  and the emitter work function  $\phi_e$  are in  $V/\text{\AA}$  and eV, respectively. The maximum emitter current  $I_o$  in Eq. (1) is given by the well known Fowler-Nordheim equation

$$I_o = \frac{e^3 F^2 A_o}{8\pi h \phi_e^2 t^2(y)} \exp[-4(2m\phi_e^3)^{1/2} v(y)/3\hbar e F] \quad (3)$$

$$= \frac{1.5 \times 10^{10}}{\phi_e^2 t^2(y)} F^2 A_o \exp[-0.683 \phi_e^{3/2} v(y)/F] \text{ (A)}$$

where  $A_o$  is the area of the emitting surface from which the collected current originates. The image correction terms  $t(y)$  and  $v(y)$  are slowly varying tabulated functions of the auxiliary variable  $y = (e^3 F)^{1/2} / \phi_e$ .<sup>11</sup>

From Eq. (1), it is apparent the  $dI_c/d\varepsilon$  turns on abruptly at the emitter Fermi level when  $p$  is small and decays exponentially with decreasing electron energy. The value of the half width  $\Delta$  of the TED can be obtained from Eq. (1) so that at  $p = 0$ ,  $\Delta$  is given by

$$\Delta = 0.69d. \quad (4)$$

Since the practical value of  $d$  varies from 0.1 to 0.3 eV, the experimental half widths fall in the range 0.07 to 0.2 eV.

For the retarding potential method, as diagrammed in Fig. 1, the emitted electrons can be collected at a metal surface of work function  $\phi_c$  only if their total energy  $E$  meets the condition

$$E > \phi_c + E_f - V_c$$

where  $V_c$  is the emitter-to-collector bias potential; thus, decreasing  $V_c$  allows all electrons down to the energy level  $\varepsilon = \phi_c - V_c$  to be collected at 0°K. The condition  $V_c = \phi_c$  represents the current cutoff since electronic states above  $E_f$  are not populated, and the total collected current  $I_c$  at a specified value of  $\varepsilon$  is given by

$$I_c = \frac{I_o}{d} \int_{\varepsilon}^{\phi_c} e^{-\varepsilon/d} d\varepsilon = I_o (1 - e^{-\varepsilon/d}). \quad (5)$$

By rewriting Eq. (5) in the working form

$$\log_{10}(I_o - I_c)/I_o = \phi_c/2.3d - V_c/2.3d \quad (6)$$

it is clear that the values of  $\phi_c$  and  $d$  can be obtained from the intercept and slope respectively of a plot of  $\log_{10}(I_0 - I_c)/I_c$  versus  $V_c$ .

At emitter temperatures above  $0^\circ\text{K}$   $\log \Delta I/I_0$  versus  $V_c$  deviates from linearity due to the Boltzman distribution of electrons in states above  $E_f$ . The theoretically expected effect of temperature on the TED has been verified experimentally and is of little consequence to the accuracy of utilizing Eq. (6) to obtain  $\phi_c$  at  $T \leq 300^\circ\text{K}$ . This can be verified by noting that the temperature accounts for only a small deviation from linearity in the  $\log \Delta I/I_0$  versus  $V_c$  plot near  $V_c = \phi_c$  as shown in Fig. 2.

Alternatively, one may obtain  $\phi_c$  by noting that the value of  $V_c$  at  $I_c/I_0 = 0.5$  when inserted into Eq. (6) yields

$$\phi_c = V_c(1/2) - d \ln 2 \quad (7)$$

where  $V_c(1/2)$  is the value of  $V_c$  for which  $I_c/I_0 = 0.5$ . Eq. (7) is strictly applicable only for  $T = 0^\circ\text{K}$ ; however, the temperature correction to  $V_c(1/2)$  is minor and only amounts to  $\sim 10$  meV at  $300^\circ\text{K}$ . The principal source of experimental error in this method stems from the uncertainty in the experimental values of  $d$  and  $I_0$  due to electron reflection. This is discussed in greater detail in the next section.

Eq. (1) may be differentiated with respect to  $\epsilon$  in order to obtain the difference in energy  $\epsilon_p$  between the peak of the TED and the Fermi energy level:

$$\epsilon_p = kT \ln \frac{kT}{d - kT} \quad (8)$$

This equation, plotted in Fig. 3 at several values of  $d$ , may be used to obtain the theoretical value of  $\epsilon_p$  which is equal to  $\phi_c - V_p$ . Since  $V_p$  (the position of maximum  $dI_c/dV_c$  on the energy axis) can be obtained experimentally, the value of  $\phi_c$  can be obtained directly from the TED curve and Fig. 3. Since in practice  $\epsilon_p \approx 30$  mV this method gives  $\phi_c$  easily within 1% accuracy.

Even though the assumptions of the Sommerfeld free electron model, upon which Eq. (1) and the subsequent equations are based has recently been found to be inadequate for certain crystallographic directions of tungsten<sup>2</sup> and molybdenum<sup>3</sup>, the occurrence of the emission threshold at  $E_f$  was unchanged for clean emitters. In any case, inadequacies in Eq. (1) due to band structure effects can be easily avoided for this application by choosing an emission direction (e.g., the  $\langle 111 \rangle$  or  $\langle 310 \rangle$  of tungsten) for which the corresponding TED curve agrees well with Eq. (1). For that reason we have utilized for this study oriented field emitters with these directions along the emission axis. Thus, all that must be known concerning the emitter in order to apply the FERP method of work function determination is the value of  $d$  which can either be calculated with sufficient accuracy from the  $I(V)$  characteristics of the emitter using Eq. (2) or determined experimentally from Eq. (6).

### ELECTRON REFLECTION

Only one property of the collector that can detract from the complete applicability of the above equations in evaluating  $\phi_c$  is electron

reflection near the threshold of collection, which cannot be eliminated by the FERP method should it occur. We can indicate the effect of reflection on Eq. (1) by noting that  $I_c = I_p(1-R)$ , where  $I_p$  is the primary beam current impinging on the collector, and by defining the energy dependent reflection coefficient  $R(\epsilon)$  as  $R(\epsilon) = I_r/I_p$ , where  $I_r$  is the reflected current. With these definitions one may readily show that the experimentally measured quantity  $dI_c/d\epsilon$  is given by

$$dI_c/d\epsilon = \alpha(\epsilon) dI_p/d\epsilon - I_p d\alpha/d\epsilon \quad (9)$$

where  $\alpha(\epsilon) = 1 - R(\epsilon)$  is the electron acceptance coefficient and  $\epsilon = |\phi_c - V_c|$  is the maximum kinetic energy of the collected electrons. Near the collection current threshold (i.e.,  $\epsilon \sim 0$ ) the last term of Eq. (9) will be small compared to the first since  $I_p \rightarrow 0$  as  $\epsilon \rightarrow 0$  and  $d\alpha/d\epsilon$  is normally small at  $\epsilon = 0$ .

However, as the energy of the primary electron beam increases above the threshold voltage considerable change may occur in  $\alpha(\epsilon)$  (i.e.,  $d\alpha/d\epsilon$  becomes large) which in turn will cause serious deviation in the apparent value of  $I_p$ . Thus, plotting the data according to Eq. (6) in order to obtain an accurate value of  $\phi_c$  and  $d$  will not be possible. In like manner it will be difficult to utilize Eq. (7) in order to obtain  $\phi_c$  due to the inability to obtain an accurate value of  $I_0$ .

In contrast, Eq. (8) is basically unaffected by reflection since the last term of Eq. (9) can usually be neglected at  $\epsilon = \epsilon_p$ . We should

also point out that a cursory examination of Fig. 3 reveals that  $\epsilon_p$  is very small (less than 40 mV) at practical values of  $d$  and  $T$  so that uncertainties in the exact position of  $\epsilon_p$  due to reflection will not introduce appreciable error in the value of  $\phi_c$ . Thus, in the event that detectable reflection should occur for a particular collector at threshold the evaluation of  $\phi_c$  should be accomplished from the TED curve through Eq. (8).

### EXPERIMENTAL APPROACH

The basic requirement of the electron optical system for this application is to transform the highly divergent electron beam into a co-linear beam normal to the collector substrate surface and to simultaneously decelerate it to zero volts. In order to maximize the analyzer energy resolution the electron source must be highly apertured<sup>12</sup> which in turn causes a very low beam transmission coefficient of the order of  $10^{-3}$  to  $10^{-4}$ . However, if the emitter is to be operated at room temperature the resolution of the analyzer need only be  $\sim 100$  mV<sup>13</sup>; therefore, an electron optical system which sacrificed unnecessary resolution was designed for this application in order to obtain a larger collector current to speed the data acquisition. Rather than aperture the primary beam to the usual  $\sim 1^\circ$  half angle  $\theta$  in order to maximize resolution, we chose for this application  $\theta \approx 8^\circ$ ; depending on the orientation of the emitter this aperture angle allowed a beam transmission of the order of 10%.

Currents in the  $10^{-7}$  A range were easily obtained in the focused spot thereby allowing the gun to be used as an electron source for other applications as well.

The electrostatic focusing system used in the analyzer shown in Fig. 4 consists of an anode, two Einzel lenses and a 500 line/in decelerating mesh electrode which established parallel equipotential surfaces in front of the collector. All electrodes were made from molybdenum. A two stage electrostatic focusing system with a virtual cross-over in front of the first lens was chosen over a single stage because of its greater optical efficiency. The lens circuitry is shown in Fig. 5, and the lens operating voltages given in Table I were arrived at by analytical computer analysis and confirmed experimentally. The anode electrode controls the emission level; varying the voltages on the downstream focusing electrodes have negligible effect upon the emission current. As the beam enters the first einzel lens it is partially decelerated and forms a virtual image of the source  $\sim 2\text{mm}$  behind the emitter tip. The second Einzel lens focuses the virtual tip image into a  $\sim 0.5\text{ mm}$  spot size at the mesh electrode  $E_9$ . Further deceleration occurs between electrode  $E_8$  and the mesh  $E_9$ . In most cases the mesh was operated between 5 and 10 V relative to the collector thereby providing a nearly field free region between the mesh and the collector at the current threshold. Examination of the spatial characteristics of the beam showed that no significant space charge expansion of the beam occurred down to the cut-off voltage of the mesh. By varying the screen voltage to lower

values and measuring the transmitted current in a Faraday cage, the energy distribution curve of the electron beam passing through the mesh was found to be in agreement with the theoretical shape. Also, from the position of the current threshold the mesh work function was found to be approximately 4.6 eV.

The lens system was aligned and mounted securely on four longitudinal glass rods. Both the emitter and anode could be removed as a unit from the tubular anode holder. In this way the emitter, which was held in place by a Corning 1720 glass bead in a molybdenum tube, could be easily replaced and prealigned in the center of the 10 mil anode aperture prior to insertion into the anode holder. By positioning the emitter in the plane of the anode aperture, no interception of the primary beam occurred at the anode or subsequent elements of the first lens. Aperturing occurred in the nearly field free region of the second Einzel lens by placing two 40 mil diameter stops in the last lens tube. Thus, electron induced desorbed ions or neutrals from the anode was eliminated and the high positive potential saddle at the anode prevented ions generated beyond the first aperture from bombarding the cathode. This design feature greatly improved the current stability without requiring rigorous outgassing of the electrodes. The angular convergence of the beam at the collector was fixed by geometry to be  $< 1.4^\circ$  for a well focused spot. Hence, negligible loss in resolution resulted from the angular deviation of the beam from perpendicularity at the collector.

The large aperture angle of the analyzer necessarily reduced the resolution of the tube as a retarding energy analyzer. Using the voltage separation between the 10 and 90% points on the leading edge of the energy distribution as described by Young and Kuyatt<sup>13</sup>, the resolution of the gun was determined to be 50 to 80 mV. This resolution was adequate to resolve the leading edge of the energy distribution curve at room temperature.

The emitter orientations selected for the field electron source in this study were  $\langle 111 \rangle$  and  $\langle 310 \rangle$  tungsten, fabricated from zone oriented wire. Previous studies<sup>2</sup> have shown that electrons field emitted from these orientations exhibit energy distribution curves that agree closely with the Sommerfeld free electron model upon which the theoretical expressions of the previous section are based. Furthermore, the work functions of the crystal planes intersecting these directions are quite low -- 4.3 eV for the (310) plane and 4.4 eV for the (111) plane -- thereby providing the highest beam transmission values.

The single crystal collector substrates of this study were shaped and mounted in the holder as shown in Fig. 4. The face of the collector crystal was circular with a diameter of 200 mils. This was sufficiently large compared to the 20 to 40 mil beam size to eliminate edge effects. Thermal and electron induced desorption cleaning of impurities at the collector crystal were accomplished through electron bombardment. Collector crystals could be easily replaced by removing the glass seal which holds the collector support rod.

## EXPERIMENTAL PROCEDURE

The single crystal collector surfaces were fabricated from MARZ grade material by a high speed grinding wheel and electro-chemical machining techniques. Several mils of the collector surface were removed by electrochemical etching in order to eliminate mechanical defects. The etchant solutions for the nickel, copper, tungsten, niobium and iridium surfaces were concentrated phosphoric acid for both nickel and copper, sodium hydroxide, 25% hydrofluoric/25% sulfuric acid solution in water, and 5% sodium hypochlorite, respectively. The alignment of the desired crystal directions with respect to target normal was within  $\pm 1^\circ$  as shown by Laue x-ray examination. Monocrystallinity of the substrates was carefully checked both before and after measurement by a high powered optical microscope and Laue x-ray examination.

After mounting the collector substrate, the tube was evacuated to  $10^{-10}$  torr pressure range. The arrangement allowed for the option of immersing the tube partially or completely in liquid nitrogen in order to enhance vacuum stability and to extend the temperature range of the work function measurements.

Cleaning of the crystal surface was accomplished by electron bombardment heating to  $2100^\circ\text{K}$  for niobium and tungsten,  $1700^\circ\text{K}$  in the case of iridium,  $1400^\circ\text{K}$  for nickel and  $1100^\circ\text{K}$  for copper. The copper crystal was exposed to  $10^{-6}$  torr of hydrogen and heated to

1250°K. In order to remove potential carbon contamination the nickel crystal was first heated in  $10^{-5}$  torr of oxygen followed by heating in  $10^{-6}$  torr of hydrogen and then heated to  $\sim 1400^\circ\text{K}$  in high vacuum.

Thermal heating was continued until the field electron emitter, which was also cleaned thermally, and therefore very sensitive to gas release from the collector, showed no change in current after flashing the collector substrate to its cleaning temperature. As a corollary check, the absence of further change in the collector work function on heating was used as an indication of a clean surface.

The emitter-to-collector current-voltage characteristics were taken several times for each collector crystal and plotted on an x-y recorder. A computer program was formulated to plot the data according to Eq. (6) so that a value of  $\phi_c$  and  $d$  could be obtained. As will be noted later in the paper this method of determining  $\phi_c$  and  $d$  was not always applicable due to reflection. Therefore, the differential curve was also taken by utilizing the position 3 circuitry shown in Fig. 5, which involves the well known electronic differentiation method utilizing a PAR HR-8 Lock-In Amplifier. A 10 mV 1000 Hz signal  $v_s$  was fed to the emitter through the transformer  $T_3$ . The magnitude of this signal detected by the Lock-In Amplifier (LA) is proportional to  $dI_c/dV$ . From the position of the TED peak and Eq. (8), a value of  $\phi_c$  was obtained; this result could be obtained with an experimental accuracy of  $\pm 20$  mV. The I-V and TED data were usually taken at emitter temperatures of 77 and 300°K.

## EXPERIMENTAL RESULTS

The values of  $\phi_c$  obtained by the FERP method are reported in Table II along with a comparison with other methods. These values were obtained via Eq. (8) from the TED curves shown in Figs.6-8. An interesting feature of these results is the additional structure in the TED for Cu(100), Nb(100) and to a lesser degree for Ir (111). This anomalous structure near the threshold of the TED curve was not as apparent in the other results and was determined to be due to unusual electron reflection. The integral current-voltage characteristics shown in Figs. 9-16 on a compressed voltage scale clearly show that the origin of the TED structure in Cu(100) and Ir(111) is due to electron reflection which varies rapidly at the threshold voltage. Although the integral curve for Nb(100) was not obtained due to inadvertent melting of the crystal, the structure in the TED curve suggest a reflection coefficient which also varies rapidly near threshold. All other substrates show reflection at threshold, but to a lesser degree.

If we assume that all the reflected electrons are collected at the mesh the sum of the collector current  $I_c$  and mesh current  $I_s$  is given by

$$I_p' = I_c + I_s \quad (10)$$

where  $I_p'$  is the emitter current arriving at the mesh. Noting that the

mesh transmission is given by  $I_p'/I_p = T$ , where  $I_p'$  is the current impinging on the collector, and that  $(1-R) = I_c/I_p$ , one obtains

$$(1-R) = I_c/T(I_c + I_s). \quad (11)$$

Since  $T$ ,  $I_c$  and  $I_s$  are measurable quantities  $R$  may be determined as a function of  $V_c$  as shown in Figs. 9-16 for each of the substrates. It is important to point out that Eq. (11) is valid when  $I_p$  is at its saturated value. Since we do not wish to count electrons reflected by the retarding field, it is necessary to use the theoretical variation of  $I_p$  with  $V_c$  to calculate  $R$  in the retarding range. As a self consistent check on the electron current accounting we can also measure  $I_p'$  in the deep retarding range preceding the threshold where  $I_p' = I_s$ ; this value of  $I_p'$  generally agreed with that calculated from Eq. (10) at saturation. The theoretical dependence of the current  $I_p$  on  $V_c$  is also plotted in Figs. 9-16 with appropriate normalization factors applied. Clearly the values of  $R$  for both Ir(111) and Cu(100) are unusually high and rapidly changing near threshold. It must be remembered that the energy spread of the primary beam at half height is  $\sim 0.2$  eV so that structure in  $R$  less than 0.2 eV width may be detected but not accurately reproduced with respect to shape. However, with these definitions in mind, one may confidently measure  $R$  down to zero primary beam energy. It should be pointed out that in order to obtain the value of primary beam energy  $\phi_c$  must be subtracted from the abscissa of each of the I-V curves. The latter correction has been made in Figs. 9-16.

In our experimental setup when  $V_c - \phi_c > V_s - \phi_s$  (s refers to the screen-mesh electrode) those reflected electrons which lose energy through inelastic processes will not be collected at the mesh but instead will be returned to the collector. Thus, by fixing  $V_s \approx 5.8$  V only specularly reflected elastically scattered electrons will escape from the collector crystal. The elastically reflected electron coefficient  $R_e$  has been measured for several substrates as given in Figs. 10-15. By setting  $V_s \approx 130$  V all reflected electrons in the energy range investigated return to the mesh and total reflection  $R_t$  curves are obtained (see Fig. 10). Hence, it is possible by this technique to measure the inelastically reflected electron coefficient  $R_{in}$  by noting that  $R_{in} = R_t - R_e$ . In Figs. 11-15 values of  $R_{in}$  are given for several of the crystal faces. For the crystal faces Cu(100) and W(111) only  $R_t$  values were obtained. Difficulty with leakage current to the mesh electrode caused some minor uncertainty regarding the absolute values of R for Ir(110), W(110) and Cu(100).

## DISCUSSION

### Work Function

As shown in Fig. 6 and Table II the work function values of 4.47, 4.63 and 5.25 eV obtained for the (111), (100) and (110) planes of tungsten are in close agreement with values reported by other methods, particularly thermionic and field electron emission methods. Since the electron reflection coefficient is low (less than 15%) near threshold

for the tungsten results, the values of  $\phi_c$  obtained from Eq. (6) compare within experimental error with the values computed from the TED curves via Eq. (8) (see Fig. 2 for a typical result utilizing Eq. (6)). This merely provides the expected self consistent check on the experimental method when R is small or a slowly varying function of energy near threshold.

Notable, is the well known discrepancy between  $\phi(110)$  obtained on macroscopic crystals and microscopic crystals employed in field emission (i. e., by use of the Fowler-Nordheim (FN) equation) techniques. This discrepancy is believed to be due to large geometric facets which occur on W(110) planes of a field emitter and which can alter the FN results in the observed fashion. Tungsten work function values exhibit the usual increase with surface atom density in accordance with the semiquantitative theoretical expectations of Smoluchowski.<sup>21</sup>

The Ir(111) plane, possessing one of the highest atom densities, yields the expected high work function value  $\phi = 5.76$  eV as shown in Fig. 8. A similar high value of  $\phi$  for Ir(111), in remarkable agreement with the value obtained here, has been reported by Zandberg<sup>15</sup> who observes this to be the highest work function value reported for a macroscopic single crystal metal surface. The agreement is surprising in view of the initial polycrystalline nature of Zandberg's iridium crystal. Our results indicate that this crystal face is relatively stable with respect to thermal induced recrystallization and faceting effects such as observed on the high work function Re(0001)<sup>19</sup> face.

The Ir(110) work function is somewhat lower than Ir (111) as expected on the basis of the lower atom density. Considering that the (110) face of Ir is the third most densely packed plane, the relatively large value  $\phi = 5.42$  eV is indicative of the generally high work function of all crystal faces of Ir.

The value of  $\phi = 4.18$  eV for the (100) face of bcc niobium shown in Fig. 7 agrees closely with thermionic and FN values reported by others.<sup>16, 17</sup> (See Table II). The work function values for W(100) and Mo(100) obtained by a variety of methods indicate best values of 4.65 and 4.40 eV respectively.<sup>17</sup> Both W(100) and Mo(100) possess identical atom densities  $\sigma = 10.9 \times 10^{14}$  atoms/cm<sup>2</sup>. Since Mo and Nb are neighboring elements in the periodic table one might expect geometric factors to dominate thereby causing a larger  $\phi$  for Nb. This is obviously not the case. These results underscore the role of electronic factors in the variation of work function with crystal face and material.

Few reliable values of work function for the (100) face of Ni and Cu are reported in the literature - obviously, due to the surface cleaning difficulties. Our results, shown in Fig. 7 and Table II are in rough agreement with photo electric<sup>18</sup> and thermionic<sup>20</sup> values reported for Ni(100) and Cu(100) respectively. Using careful cleaning procedures and a gold reference electrode, Delchar<sup>22</sup> reports a work function value of 5.16 eV for Cu(100) in excellent agreement with this work. Delchar points out that any possible error in the work function value for the reference electrode would likely be in such a direction as to raise the Cu(100) value.

Our value of Ni(100) work function is 0.30 eV larger than other reliable measurements. Most previous measurements on crystals of questionable surface purity converge on a value of 4.9 eV. Clearly, a combination of the FERP method with Auger analysis would be extremely helpful in answering the question of surface cleanliness.

It is interesting to note that the elements Cu and Mo are each adjacent to Ni and Nb respectively in the periodic table. In each case the change in the free atom electronic structure between adjacent elements involves the filling the inner d orbitals. In the case of the fcc metals Ni and Cu the work function of the (100) crystal face decreases with atomic number  $Z$ , whereas with the bcc metals Nb and Mo the work function of the (100) face increases with  $Z$ . At the same time each of these pairs of metals exhibit a slight increase in their respective lattice constants with  $Z$ . The value of the (100) work function for the bcc metal W is larger than the Mo value by  $\approx 0.25$  eV even though both metals possess nearly identical lattice constants and differ in electronic structure by the filling of inner 5p and 4f orbitals. Clearly, a predictive theory of metallic work function must include complex structural and electronic factors.

### Electron reflection

The simultaneous measurement of work function and electron reflection was undertaken here primarily as a further index of surface cleanliness. The ease of separating the elastic  $R_e$  and inelastic  $R_{in}$

reflection coefficients by this method motivated a more detailed study of these coefficients as a function of the primary electron energy  $E_p$ . Several interesting and surprising features have been observed in the variation of  $R$  with  $E_p$  in the low energy range.

Fig. 9 shows that the variation of  $R_t$  with  $E_p$  for W(111) is in good agreement with careful measurements of  $R_e$  by Armstrong.<sup>23</sup> Because of the ability of the FERP method to accurately measure  $R$  to within a few tenths eV of threshold our results show a definite peak at 3 eV heretofore unobserved. A small peak observed at 6 eV is in agreement with Armstrong's results. Disagreement in absolute scale at larger values of  $E_p$  can be ascribed to the difference between Armstrong's measurement of  $R_e$  and in this work the measurement of  $R_t$  for this crystal face. As also shown in Armstrong's results surface contamination markedly alters  $R_e$ ; thus the close agreement between the two results mutually supports the claim of an atomically clean surface.

The W(100) results in Figs. 10 and 11 show the experimental variation of  $I_c$  with  $E_p$  for  $V_B = 100$  and 5.25 V respectively, thereby illustrating the difference between the total and elastic reflection modes. In Fig. 11 the value of the experimental reflection coefficients  $R_{in}$  and  $R_e$  are given along with Armstrong's results for  $R_e$ . Both results agree that a sharp peak in  $R_e$  occurs between 3.5 and 4.0 eV as observed similarly in the W(111) results. In disagreement with Armstrong's results, the large peak in  $R_e$  at 8.0 eV is missing and instead a smaller peak at 6.5 eV appears. In addition, a major peak observed in our results, but

absent in Armstrong's, occurs at 16.5 eV\*. Both investigations agree on a broad peak in  $R_e$  at 10.5 eV. Differences in the  $R_e$  vs  $E_p$  curves obtained in the two investigations must be ascribed to either a small degree of surface contamination, crystal inhomogeneity or experimental artifact.

The variation of  $R_e$  with  $E_p$  for W(110) shown in Fig. 12 over a wider  $E_p$  range exhibits a large peak modulated with fine structure in the 4-6 eV range. Lesser peaks occur at 14 and 27 eV as  $R_e$  decreases from a peak value of 0.34 at 5 eV to less than 0.03 at 75 eV. The W(110)  $R_e$  curve agrees closely with an earlier result by Kahn, et. al.<sup>24</sup>

The inelastic reflection coefficients  $R_{in}$  given in Figs. 11 and 12 for W(100) and W(110) exhibit very similar structure for both crystal faces. That is, each exhibits an onset threshold at 3 eV, fine structure in the 3 to 10 eV range, and additional peaks at 12 and 17 eV. The larger range of  $E_p$  for W(110) indicates an increase in  $R_{in}$  to a value of 0.47 at 52 eV where it then begins a slight drop. The  $R_e$  and  $R_{in}$  curves for W(100) and W(110) both cross in the 12 to 15 eV range and with increasing  $E_p$  the ratio  $R_{in}/R_e$  increases to a value of  $\sim 90$  at  $E_p = 60$  eV for W(110).

One of the most unusual results of this study is the exceedingly large value of  $R_e \approx 0.75$  as  $E_p \rightarrow 0$  as shown in Fig. 13 for Ir(111). The Ir(110) results in Fig. 14 measured over a larger  $E_p$  range also show an increase in  $R_e$  at threshold but not nearly as large a value as for Ir(111). From a dynamical point of view, these results suggest the occurrence of a band gap relatively free of surface states approximately 5.79 eV above

---

\*Earlier results by Kahn, Hobson and Armstrong<sup>24</sup> show a definite peak in this energy range.

the Fermi level along the  $\langle 111 \rangle$  direction of Ir. Both crystals show one additional large peak in  $R_e$  at 11.5 and 15 eV for Ir (110) and Ir (111) respectively. While, the variation of  $R_e$  with  $E_p$  differs sharply for the two crystal faces, the variation of  $R_{in}$  with  $E_p$  is quite similar. On both crystal faces  $R_{in}$  increases monotonically with  $E_p$  showing a series of small peaks in the 8 to 30 eV range. No maximum in  $R_{in}$  is apparent in this range of  $E_p$  as was the case for W(110) and Ni(100). In contrast with the W results the threshold for  $R_{in}$  occurs at a higher voltage, i. e., in the 6 to 8 eV range. It is interesting to note that whereas  $R_t$  is large for Ir(111) at  $E_p = 0$ , the value of  $R_t$  for Ir(110) is smaller at  $E_p = 0$  and increases to a value of 0.7 at 70 eV where it appears to be still increasing with  $E_p$ .

The variation of  $R_e$  with  $E_p$  for Ni(100) is in general agreement with diffraction intensity studies. The peaks in  $R_e$  at threshold 15, 28 and 38 eV have been observed elsewhere,<sup>25</sup> but with somewhat differing relative magnitudes. The peak near threshold can be ascribed to the first order primary Bragg peak of the 00 band. We also observe an increase in the elastic peak widths and decrease in the elastic peak heights as  $R_{in}$  increases in accordance with certain theoretical viewpoints of the electron scattering mechanism.<sup>25, 26, 27</sup> A large peak normally observed in  $R_e$  at 55 eV is missing in the present results. Part of the discrepancy may be due to the presence of a few grain boundaries which developed near the edge of our Ni(100) crystal prior to obtaining the reflection curves. Although the central portion of the crystal (where the electron beam impinged) appeared to be monocrystalline

(as determined by Laue x-ray), a slight reduction in  $\theta$  occurred indicating the possibility of structural effects on the reflection results.

The inelastic reflection threshold for Ni(100) occurs a few volts above zero and exceeds  $R_e$  for  $E_p > 16$  eV. A small peak in  $R_{in}$  occurs at 18 eV followed by a major maximum at 40 eV. It is clear from the Ni(100) results along with the above mentioned results that inelastic processes become important above 15 to 20 eV and must therefore be considered carefully in theoretical attempts to explain LEED intensity variations with  $E_p$ .

The Cu(100) results shown in Fig. 16 were obtained for  $R_t$  only over a limited range of  $E_p$ . Since  $R_{in}$  is likely to be small in this energy range  $R_t \approx R_e$ . Although not as large as the threshold peak for Ir(111), the threshold peak for Cu(100) is quite large and has been attributed<sup>28</sup> to the well known band gap<sup>29</sup> in the bulk  $E(k)$  diagram occurring at the vacuum level. Previous LEED studies of the specular reflectivity  $I_{00}$  from Cu(100) gave a value of  $R_e = 0.36$  around  $E_p = 1$  eV.<sup>28</sup> The results reported here agree closely with the latter results but also show a larger peak at  $E_p \approx 0$  of  $R_e = 0.47$ . In addition, a very small peak is observed at  $E_p = 2.0$  eV. These extremely narrow peaks (less than 0.5 eV) point out the resolving power of this technique near threshold and agree with the previous observation that peak widths in  $R_e$  below the onset of inelastic reflection are narrower.

## SUMMARY

The use of the FERP method to accurately measure true work function of a variety of single crystal surfaces (see Table II) with a minimum of assumptions regarding the nature of the electron emission process has been demonstrated. A combination of the FERP and LEED/Auger should provide a powerful combination of techniques to accurately and conveniently measure bare surface true work functions of conducting surfaces. The occurrence of electron reflection from the collecting surface can generally be tolerated without introducing appreciable error (ca  $\pm$  0.02 eV) provided that the work function is obtained from the peak in the TED curve. An unusually large work function of 5.76 eV for Ir(111) was obtained in agreement with an earlier result.<sup>15</sup> Other results agreed favorably with previously measured and accepted values of work function.

As shown by Armstrong<sup>23</sup> surface contamination or crystal imperfection can alter the elastic reflectivity vs. primary energy curves. We have shown that the FERP technique can yield both elastic and inelastic reflection curves accurately to within a few tenths eV of zero primary energy and thereby can be used as an indicator of surface conditions. Values of  $R_e$  and  $R_{in}$  for several crystal faces agreed reasonably well with published curves. We noted that  $R_{in} \gg R_e$  as  $E_p \gtrsim 15$  eV for most crystal faces examined. An unusually large value of  $R_e$  was obtained

for Ir (111) and Cu (100) at threshold. Whereas the structure in the  $R_e$  curves was highly dependent on crystal orientation, the  $R_{in}$  curves were generally unaltered by crystal orientation including the threshold values of  $E_p$  which were usually 3 to 8 eV.

Finally, we anticipate that the FERP technique can be profitably used to examine the combined effect of chemisorption on  $\phi$ ,  $R_e$  and  $R_{in}$ .

#### ACKNOWLEDGEMENTS

The authors gratefully acknowledge the technical assistance of Mr. Noel Martin and Mr. R. Rathkey and helpful discussions with Dr. A. E. Bell.

**Table L. Operating voltages on lens elements**  
(see Fig. 5 with emitter at 0 V).

Lens element	Operating voltage
$E_4$	$0.06E_3$
$E_5 = E_7$	0
$E_6 = E_8$	$0.04E_3$
$E_9$	5-10 or 130-150 V

Table II

Material	Atom Density (atoms/cm <sup>2</sup> )	Work Function (eV)			
		(this work)	Thermionic	Photoelectric	Field Emission (emitter values)
W(100)	14.1	5.25 ± 0.02	5.35 ± 0.05 <sup>14</sup>		5.9 ± 0.1 <sup>2</sup>
W(100)	10.0	4.63 ± 0.02	4.60 ± 0.05 <sup>14</sup>		4.70 ± 0.05 <sup>2</sup>
W(111)	5.77	4.47 ± 0.02	4.40 ± 0.02 <sup>14</sup>		4.45 ± 0.03 <sup>2</sup>
Ir(111)	15.8	5.76 ± 0.04	5.79 ± 0.03 <sup>15</sup>		
Ir(110)	9.7	5.42 ± 0.02			
Nb(100)	10.9	4.18 ± 0.02	3.95 ± 0.03 <sup>16</sup>		3.87 ± 0.01 <sup>17</sup>
Ni(100)	16.15	5.53 ± 0.05		5.22 ± 0.04 <sup>18</sup>	
Cu(100)	15.4	5.10 ± 0.05	4.9 <sup>20</sup>		

## REFERENCES

1. F.I. Itskovich, Soviet Physics JETP 23, 945, 1425 (1966); 24, 202 (1967).
2. L.W. Swanson and L.C. Crouser, Phys. Rev. 163, 662 (1967).
3. L.W. Swanson and L.C. Crouser, Phys. Rev. Letters 19, 1179 (1967).
4. R.D. Whitcutt and B.H. Blott, Phys. Rev. Letters 23, 639 (1969).
5. J.E. Henderson and R.E. Badgley, Phys. Rev. 38, 590 (1931).
6. A.A. Holscher, Surface Sci. 4, 89 (1966).
7. C. Kleint, Exp. Tech. Phys. 16, 125 (1968).
8. H. Shelton, Phys. Rev. 107, 1553 (1957).
9. R.D. Young and E.W. Müller, Phys. Rev. 113, 114 (1959).
10. A. van Oostrom, Phillips Res. Rept. Supp. (Netherlands) 11, 102 (1966).
11. R.H. Good and E.W. Müller, Handbuck der Physik, edited by S. Flugge (Springer-Verlag, Berlin, 1956), Vol. 21, p. 176.
12. T.E. Everhart, J. Appl. Phys. 38, 4944 (1967).
13. R.E. Young, and C.E. Kuyatt, Rev. Sci. Inst. 39, 1477 (1968).
14. O.D. Protopopov, E. V. Mikheeva, B.N. Sheinberg and G.N. Shuppe, Soviet Phys. - Solid State 8, 909 (1966).
15. E. Ya. Zandberg and A. Ya. Tontegode, Soviet Phys. - Solid State 12, 878 (1970).
16. O.D. Protopopov and I. V. Stringushchenko, Soviet Phys. - Solid State 10, 747 (1968).
17. A.E. Bell, C.J. Bennette, R.W. Strayer and L.W. Swanson, "Single Crystal Clean Work Functions and the Behavior of Various Adsorbates on Metal Surfaces", NASA-Lewis, Contract #Nr. NAS3-11820 (Field Emission Corporation, McMinnville, Oregon 1970).

18. B.G. Baker, B.B. Johnson and G.L.C. Maire, Surface Sci. 24, 572 (1971).
19. L.G. Feinstein and M.S. Macrakis, Surface Sci. 18, 277 (1969).
20. E.H. Blevis and C.R. Crowell, Phys. Rev. 133, 580 (1964).
21. R. Smoluchowski, Phys. Rev. 60, 661 (1941).
22. T.A. Delchar, Surface Sci. 27, 11 (1971).
23. R.A. Armstrong, Can. J. Phys. 44, 1753 (1966).
24. I.H. Khan, J.P. Hobson and R.A. Armstrong, Phys. Rev. 129, 1513 (1963).
25. S. Andersson and B. Kasemo, Surface Sci. 25, 273 (1971).
26. G. Capart, Surface Sci. 26, 429 (1971).
27. C.B. Duke, J.R. Anderson and C.W. Tucker, Jr., Surface Sci. 19, 117 (1970).
28. S. Andersson, Surface Sci. 18, 325 (1969).
29. G.A. Burdick, Phys. Rev. 129, 138 (1963).

## FIGURE CAPTIONS

- Fig. 1. Potential energy diagram for a field electron retarding potential analyzer. When the collector is biased such that only electrons from the Fermi level of the emitter can reach the collector, the battery voltage  $V_c$  is equal to the collector work function  $\phi_c$ .
- Fig. 2. Plot of  $\ln \Delta I/I_0$  vs. collector voltage for a W(110) collector. The intercept of the abscissa at  $\Delta I/I_0 = 1$  gives  $\phi_c$  according to Eq. (6).
- Fig. 3. The difference  $\epsilon_p$  in energy between the peak of the TED curve and the Fermi level as a function of T and energy parameter d.
- Fig. 4. Diagram of FERP tube showing pertinent features of the electron optical system and collector single crystal.
- Fig. 5. Diagram of the electrical circuitry associated with the FERP tube.
- Fig. 6. TED curves for W(111), W(100) and W(110).
- Fig. 7. TED curves for Cu(100), Ni(100) and Nb(100).
- Fig. 8. TED curves for Ir(111) and Ir(110).
- Fig. 9. Experimental and theoretical integral  $I(V_c)$  curves obtained from W(111). Solid line shows the total reflection curve  $R_t$ . Dashed curve gives the experimental elastic reflection curve  $R_e$  obtained by Armstrong.<sup>23</sup>

Fig. 10. Experimental and theoretical  $I(V_c)$  curves obtained for W(100).

Solid line shows the total reflection  $R_t$  curve. The mesh voltage

$V_g = 100$  V.

Fig. 11. Experimental and theoretical  $I(V_c)$  curves obtained from W(100).

Solid line curves show inelastic  $R_{in}$  and elastic  $R_e$  reflection

coefficients. The mesh voltage  $V_g = 5.25$  V.

Fig. 12. Experimental and theoretical  $I(V_c)$  curves obtained from W(110).

Solid line curves show inelastic  $R_{in}$  and elastic  $R_e$  reflection

coefficients.

Fig. 13. Experimental and theoretical  $I(V_c)$  curves obtained from Ir(111).

Solid line curves show inelastic  $R_{in}$  and elastic  $R_e$  reflection

coefficients.

d  
Fig. 14. Experimental and theoretical  $I(V_c)$  curves obtained from Ir(100).

Solid line curves show inelastic  $R_{in}$  and elastic  $R_e$  reflection

coefficients.

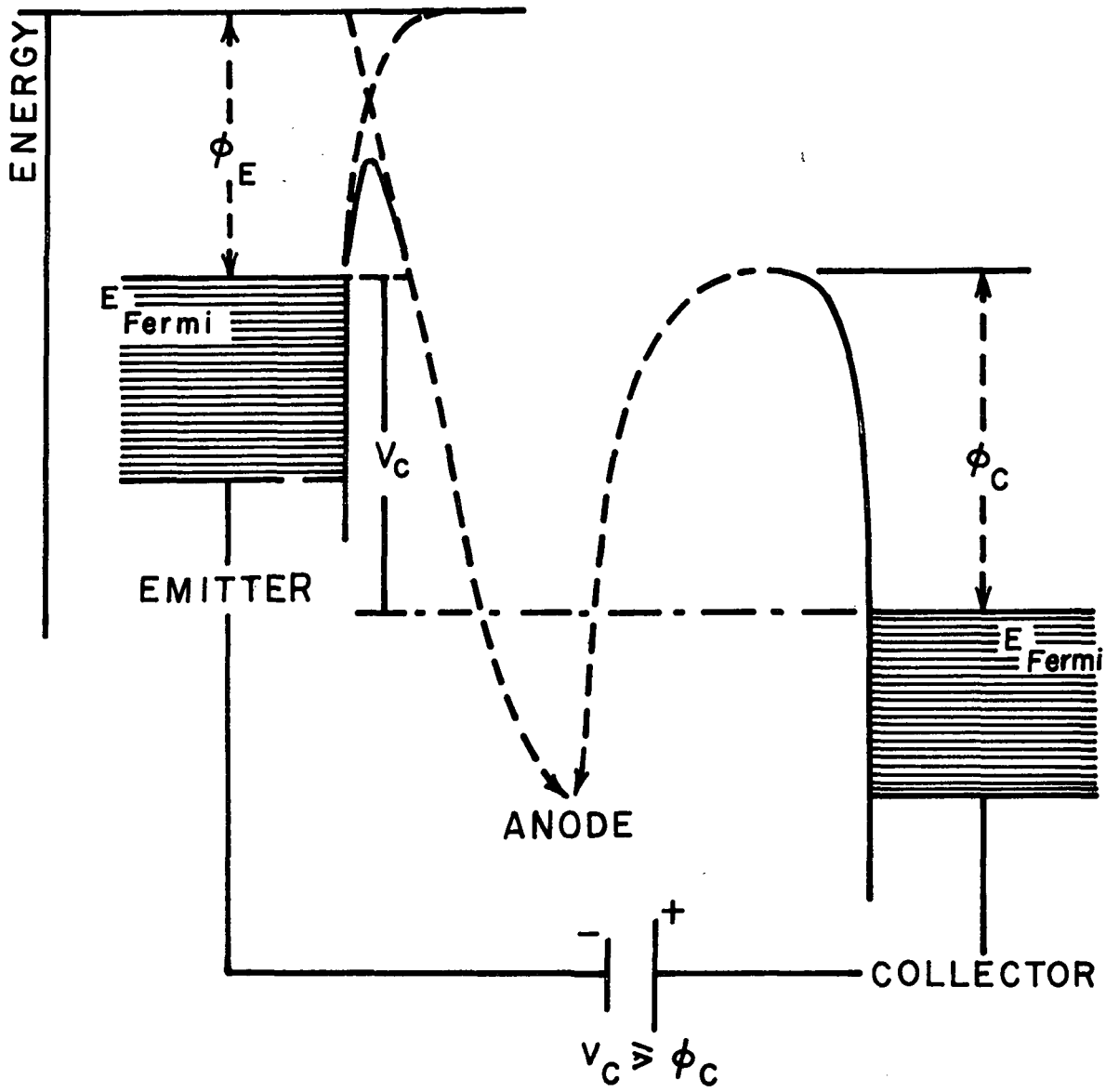
Fig. 15. Experimental and theoretical  $I(V_c)$  curves obtained from Ni(100).

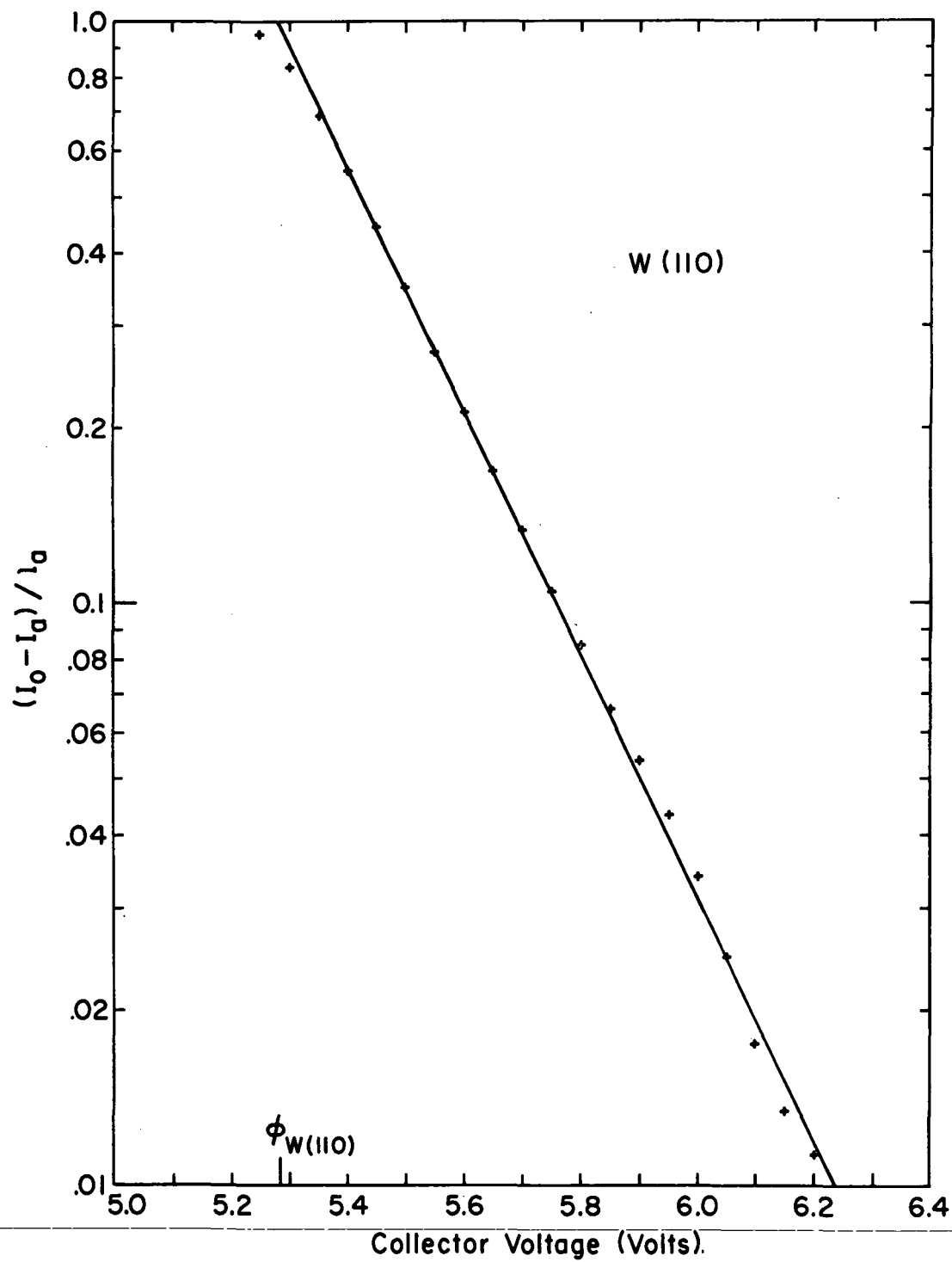
Solid line curves show inelastic  $R_{in}$  and elastic  $R_e$  reflection

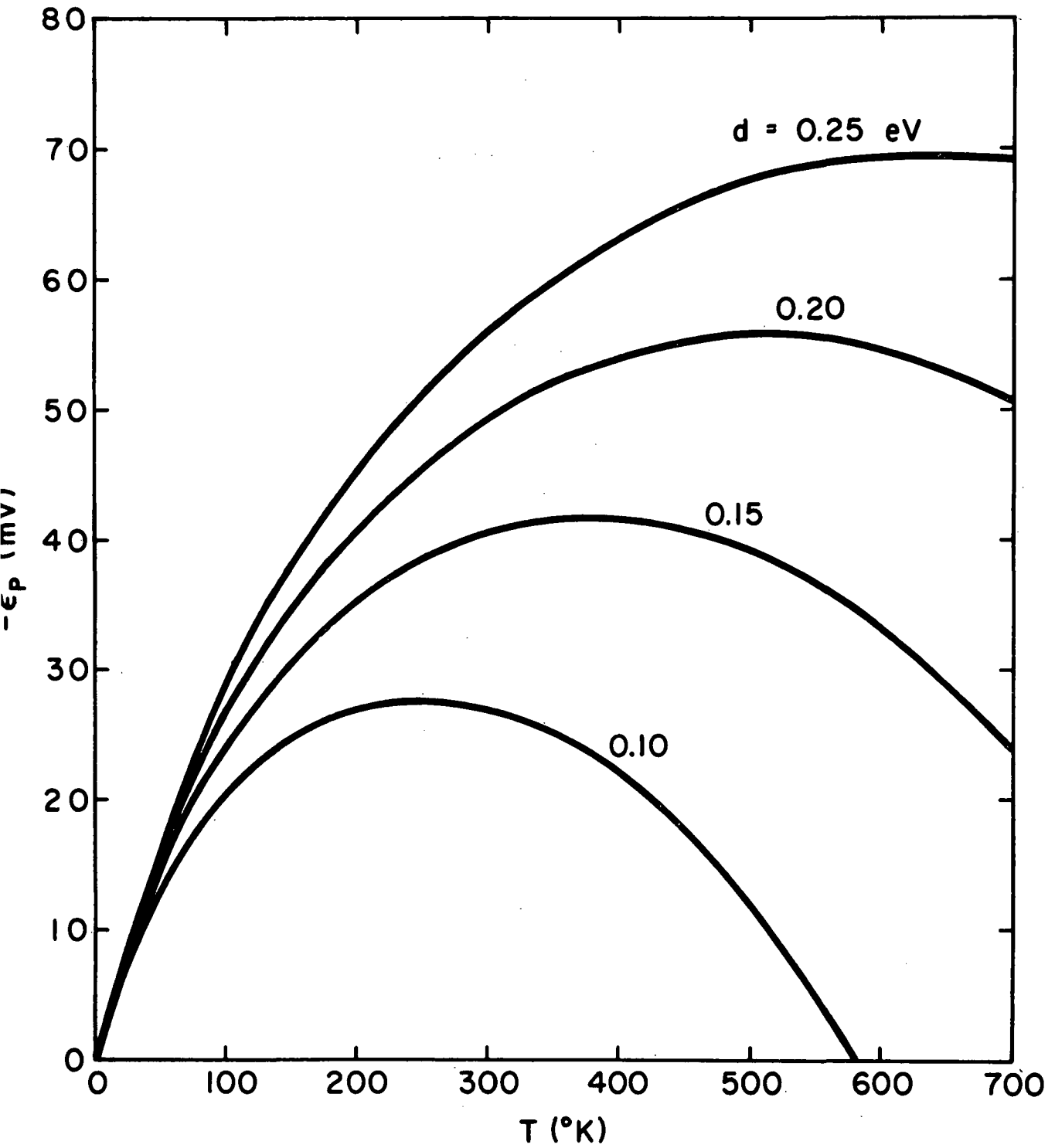
coefficients.

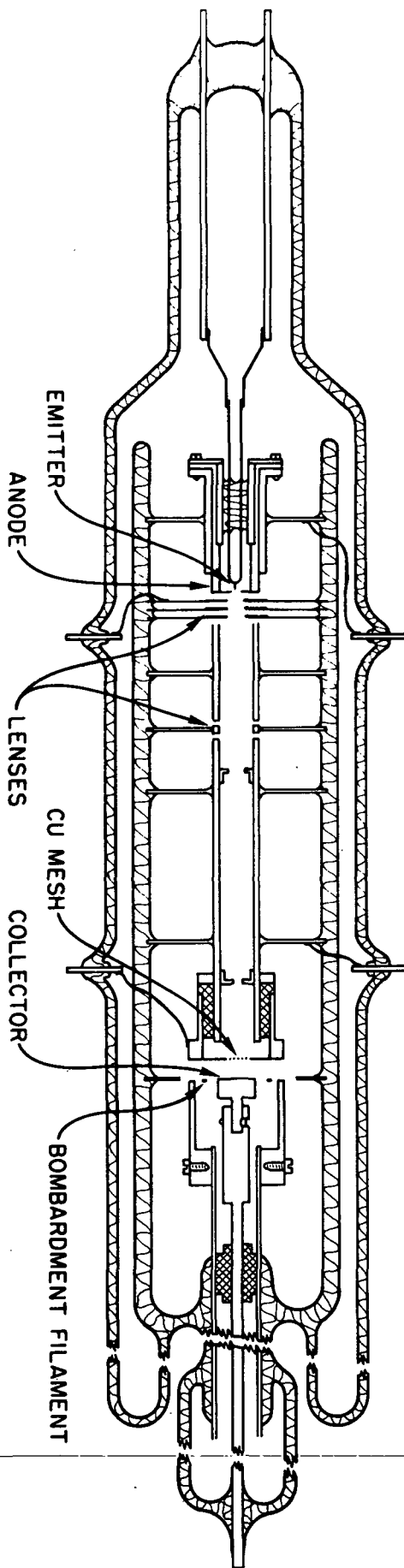
d  
Fig. 16. Experimental and theoretical  $I(V_c)$  curves obtained from Cu(100).

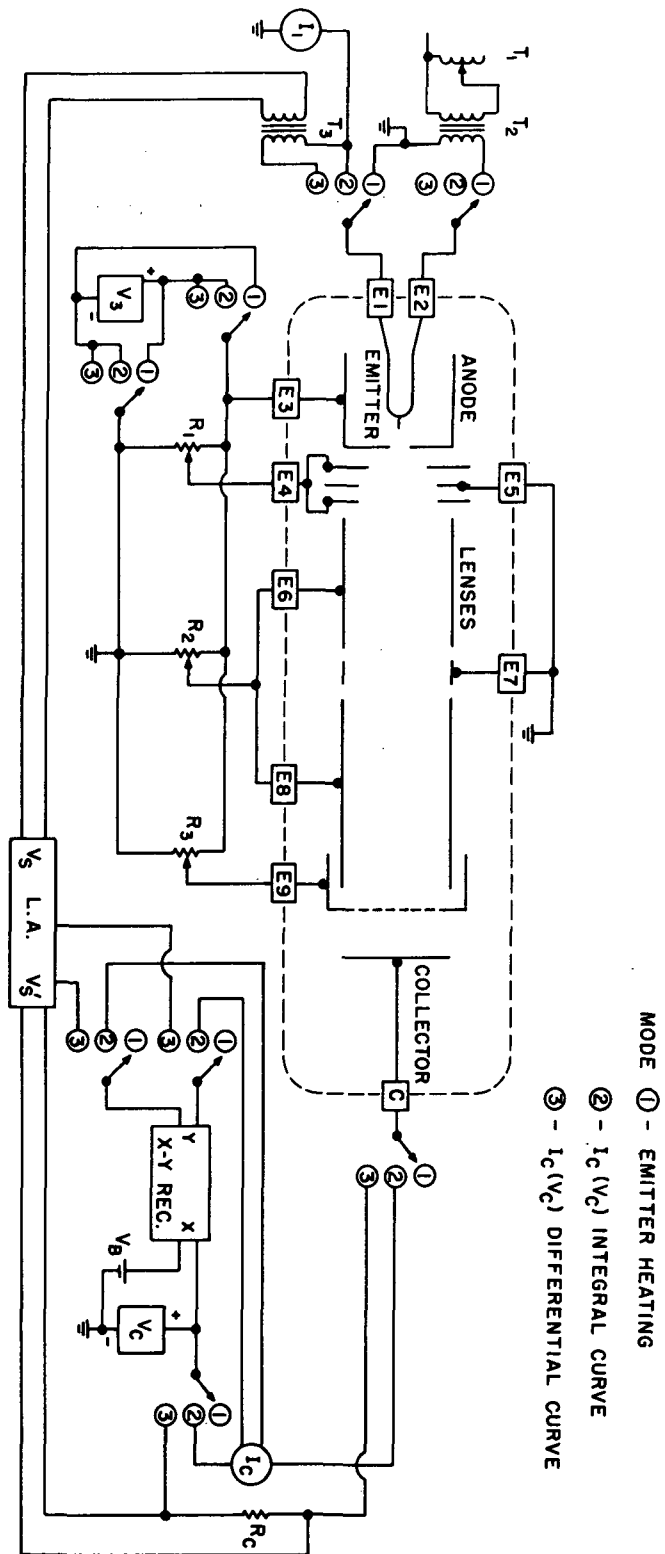
Solid line curve shows the total  $R_t$  reflection coefficient.

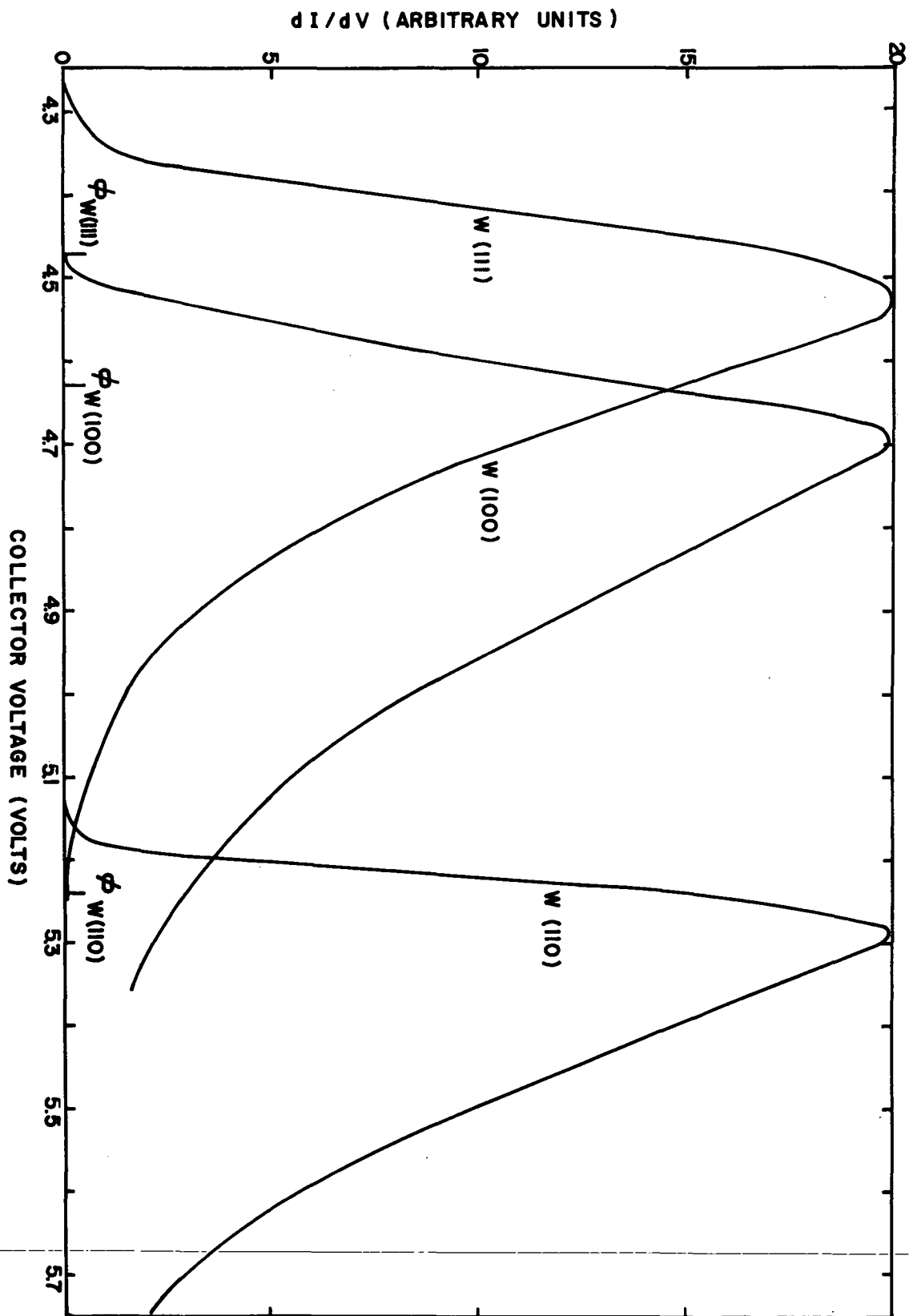


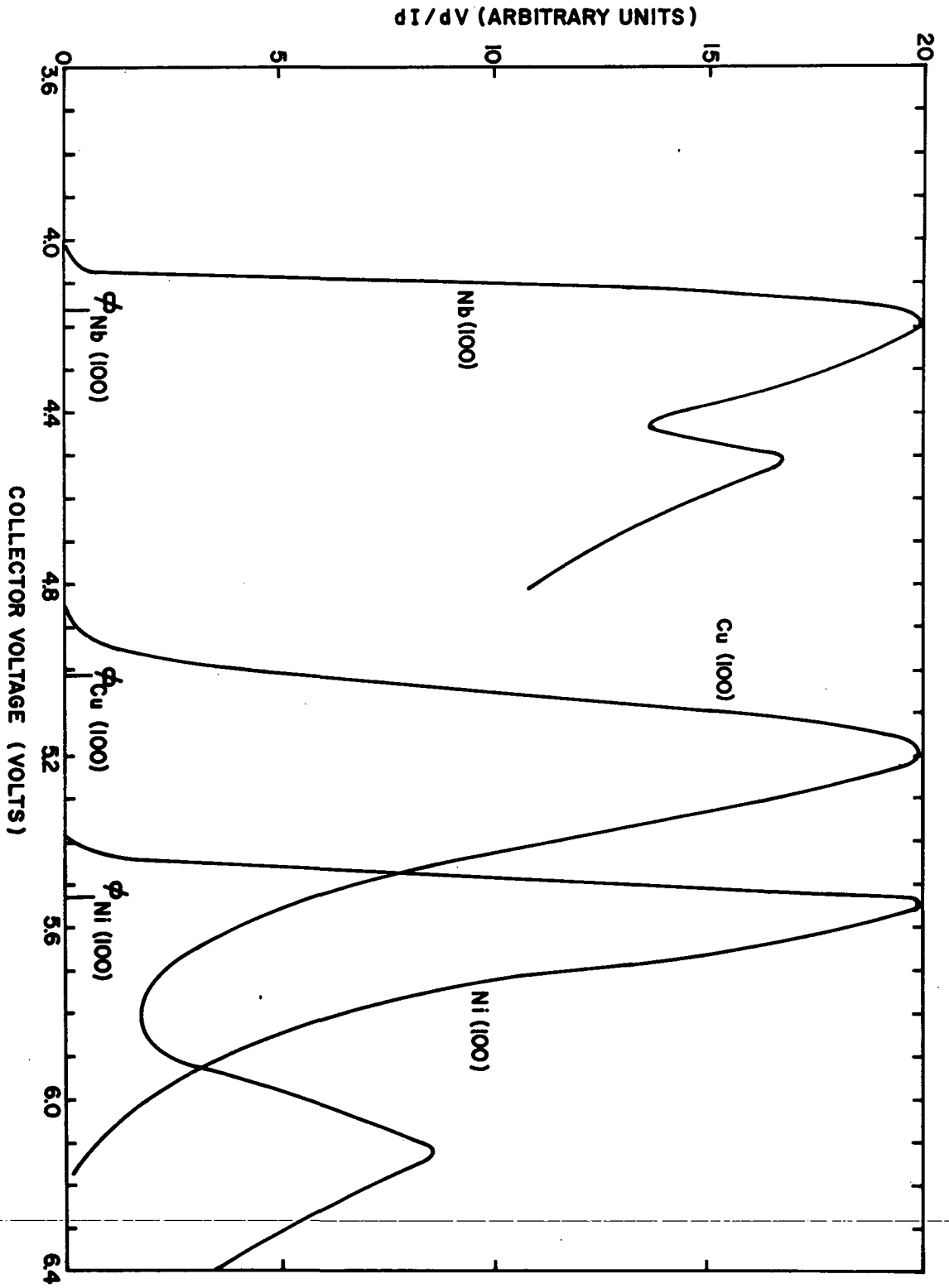












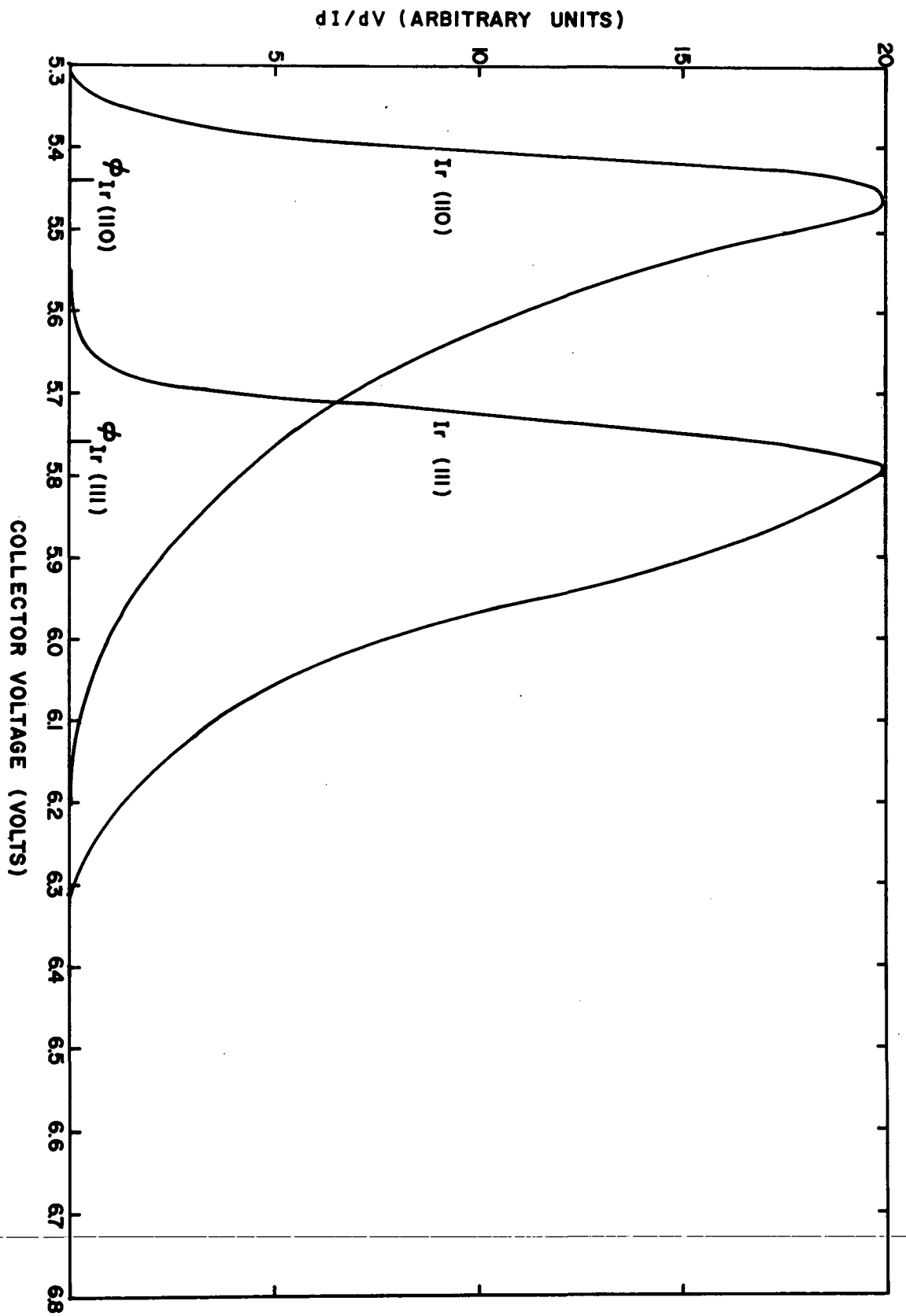


Fig. 9

